A Molecular Communication model for cellular metabolism

Zahmeeth Sakkaff[1], Andrew P. Freiburger[1], Jennie L. Catlett[2], Mikaela Cashman[3], Aditya Immaneni[3], Nicole R. Buan[2], Myra B. Cohen[3], Christopher Henry[1*], and Massimiliano Pierobon[3]

[1]Argonne National Laboratory, Data Science and Learning Division, Lemont, IL 60148 USA
[2]Department of Biochemistry, University of Nebraska, Lincoln, NE
[3]Department of Computer Science & Engineering, University of Nebraska, Lincoln, NE
[*]e-mail: cshenry@anl.gov

June 29, 2023

Abstract

Understanding cellular engagement with its environment is essential to control and monitor metabolism. Molecular Communication theory (MC) offers a computational means to identify environmental perturbations that direct or signify cellular behaviors by quantifying the information about a molecular environment that is transmitted through a metabolic system. We developed an model that integrates conventional flux balance analysis metabolic modeling (FBA) and MC, and additionally defined several channels of metabolic communication through environmental information transfers through a metabolism, to uniquely blend mechanistic biology and information theory to understand how substrate consumption is captured reaction activity, metabolite excretion, and biomass growth. The information flow in bits calculated through this workflow further determines the upper limit of information flow – the maximal effect of environmental perturbations on cellular metabolism and behaviors – since FBA simulates maximal efficiency of the metabolic system. We exemplify this method on two intestinal symbionts – *Bacteroides thetaiotaomicron* and *Methanobrevibacter smithii* – and visually consolidated the results into constellation diagrams that facilitate interpretation towards actionable design of controllable biological systems. The unique confluence of metabolic modeling and information theory in this model advances basic understanding of cellular metabolism and has applied value for the Internet of Bio-Nano Things, synthetic biology, microbial ecology, and autonomous laboratories, where the calculable control of cellular behaviors from environmental perturbations is imperative.

Keywords Molecular communication • information theory • cell metabolism • flux balance analysis • information flow

1 Introduction

Engineering biological systems and bio-nanotechnologies is essential to realize the Internet of Bio-Nano Things (IoBNT) [1], where wearable bio-computers externally monitor and direct biological systems *in situ* [2]. These external perceptions utilize biosensing [3], optogenetics [4], or magnetic nanoparticles [5], but limitations such as off-target effects on the biological system and inherent biochemical noise compromise accuracy and liability [6, 7]. The ideal method for externally perceiving a biological system would instead leverage native metabolism, and thereby minimize disturbance of the studied system: e.g. ameliorating dysbiosis by changing the chyme nutrient flows via dietary intervention [8, 9]. The lack of methods or basic knowledge of information flow from an environment to influencing behaviors – post-translation modification, signal transduction [10], gene regulation, and biomass growth [6, 11, 12] – in a metabolic network [11, 13], however, remains a bottleneck to realize this vision of environmentally controlling native metabolism [14].

Molecular communication (MC) theory in Figure S1 is an emerging confluence of communication and information theories [7, 15–17] that quantifies information flow of an environment through black-boxed channels of chemical inputs to observed outputs [18]. The information flow IF [19] through each of these channels is quantified in binary digits, or bits (1 or 0),

$$IF = H(inputs) - H(inputs, outputs) \quad (1)$$

as the excess of input uncertainty $H(inputs)$ from the output uncertainty $H(inputs, outputs)$ that depends on the inputs. Flux Balance Analysis (FBA) in Figure S2 [20], by contrast, is a metabolic modeling framework that mechanistically resolves metabolism through linear optimization and determines the profile of active metabolic reactions and maximal biomass growth for an organism in a given environment (assuming that the cell optimally acclimates [21]). FBA represents a metabolic system as a matrix S of stoichiometries

for all metabolites in all reactions and determines the profile of reaction fluxes $\frac{mmol}{hr*g_{DW}}$ as a vector $\mathbf{v}$ that represents steady-state metabolic activity ($S\mathbf{v} = 0$) [22]. FBA simulations can be tailored by changing the optimized sub-set of fluxes (conventionally those that contribute to biomass growth) and adjusting peripheral constraints on flux ranges ($\mathbf{v_{min}} \leq \mathbf{v} \leq \mathbf{v_{max}}$) that can represent the chemical effects of diverse phenomena: e.g. reaction energetics [23] or regulatory processes [24].

MC and FBA methods offer complementary value in computational biology – as methods for quantifying sensitivity to an environment and predicting mechanistic effects of an environment – however, these methods have never before been integrated into a single framework. We therefore developed such a model that couples MC and FBA to compute information flow through defined MC channels while elucidating metabolic mechanisms within each metabolic channel via FBA. We defined a comprehensive MC channel from an input of consumed substrates to externally perceived behaviors such as excretions and bimoass growth, and further partitioned this comprehensive channel into two sub-channels [25] with outputs of intermediary gene expression and the externally perceived behaviors, respectively. These channels are illustrated in Figure S3. We exemplify this unique model on two mutualistic [26] human symbionts that are associated with metabolic diseases [27, 28] – the bacterium *B. theta* and the archaeon *M. smithii* – and seven substrates that have been previously studied with these organisms [26, 29] and represent carbon, nitrogen, sulfur, and oxygen nutrient flows in chyme. These resulting information flow is visualized in constellation diagrams [30] that compresses the numerous data points from all substrate profiles to clearly reveal which profile optimally transmits information through the metabolism. This model expands basic knowledge of cellular behavior as the causal consequence of environmental substrates, and can specifically address basic questions – e.g. 1) how much environmental information can a cell encode in its metabolism? and 2) how much information about intra-cellular metabolism can be externally perceived? – as well as accelerating progress towards engineering and rationally designing biology for myriad applications from healthcare to space colonization [31, 32].

2 Methods

Figure 1 compares each of the MC channels to the metabolic processes that they represent. The defined channels include:
Stage I

$$\{U_1, U_2, ..., U_N\} \xrightarrow[\text{Consumption}]{\text{Substrate}} \{r_1, r_2, ..., r_M\} \quad , \qquad (2)$$

for the reaction activity $r_j \in [0, 1]$ for all $j \in M$ intra-cellular reactions via the consumption of $U_i \in [0, 1]$ for all $i \in N$ compounds of interest (2^N total consumption profiles);
Stage II

$$\{r_1, r_2, ..., r_M\} \xrightarrow[\text{Reactions}]{\text{Metabolic}} \{S_1, S_2, ..., S_J, Gr\} \quad , \qquad (3)$$

for externally perceived excretions $S_e \in [0, 1]$ for all $e \in E$ exchangeable compounds and biomass growth $Gr \in [0, 1]$ from metabolic activity $r_j \in [0, 1]\ \forall\ j \in M$; and **end-to-end** as the entire pipeline that conjoins the **Stage I** and **Stage II** channels. Our formulation of information flow therefore defines: $inputs = \{U_i\}_{i=1}^{N}$ and $outputs = \{r_j\}_{j=1}^{M}$ for the Stage I channel; $inputs = \{r_j\}_{j=1}^{M}$ and $outputs = \{S_e\}_{e=1}^{E}, Gr$ for the Stage II channel; and $inputs = \{U_i\}_{i=1}^{N}$ and $outputs = (\{S_e\}_{e=1}^{E}, Gr)$ for the end-to-end channel.

2.1 information flow

The input uncertainty $H(inputs)$ of eq. (1) is generally defined as

$$H(inputs) = -\sum_{i=1}^{I} (P(inputs) * \log_2(P(inputs))) \quad , \qquad (4)$$

where I is the number of unique inputs and $P()$ is a function that returns the probability of the provided argument, with all inputs and outputs being equally probable. The conditional output uncertainty $H(inputs)$ is generally defined as

$$\begin{aligned} H(inputs, outputs) = &-\sum_{o=1}^{O} (P(o)) \\ &* \sum (P(inputs, outputs) \\ &* \log_2(P(inputs, outputs)) \end{aligned} \qquad (5)$$

where O is the number of unique outputs. The $P(inputs, outputs)$ term specifically returns the probability of an output per a given input, while $P(outputs)$ returns the probability of an output among all outputs. The summations in these equations can be integrals when either the inputs or outputs are continuous; however, our strict utilization of binary variables discretizes all domains and allows summations.

The presented general expressions for $H(inputs)$ and $H(inputs, outputs)$ is tailored for FBA simulations in several dimensions. First, the terms are demarcated with an asterisk (e.g. $\{r_j^*\}_{j=1}^{M}$) to denote that the activity corresponds with the maximal possible value or theorical upper bound. Second, identical FBA solutions from different consumption profiles, based on their raw (continuous) fluxes, were grouped in Figure S4 to simplify computing IF^*. Figure S5 illustrates additional redundancy between consumption profiles as a column and the activated reactions in ≥ 1 FBA simulations as M rows.

2.2 Computational Tools and Workflow

The genome-scale models (GEMs) [33] of *B. theta* and *M. smithii*, which are detailed in Figure S6, were constructed through the KBase pipeline [34] in Figure 2. First, the organism's genome sequences from the GenBank database [35,

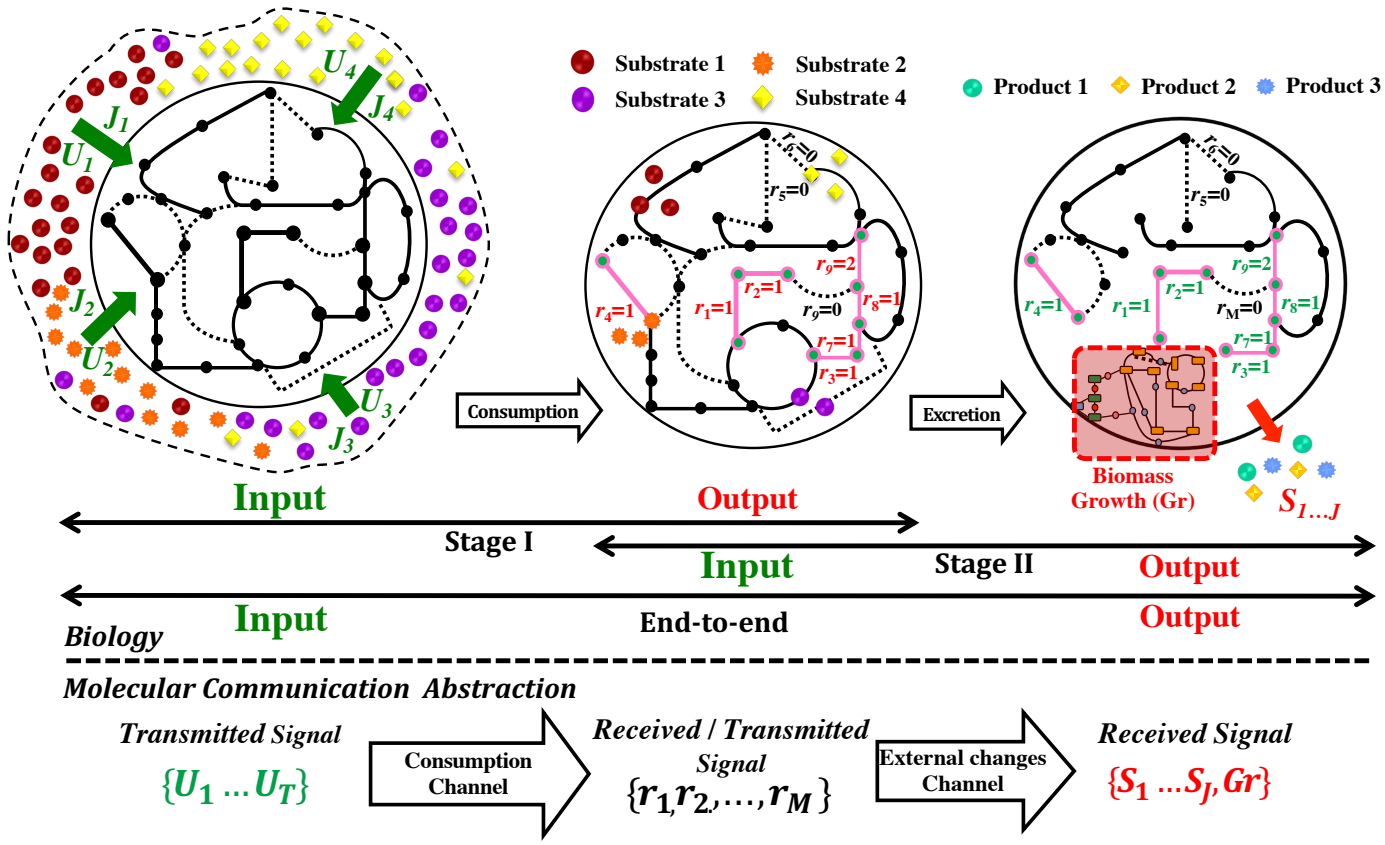

Figure 1: The molecular communication abstraction of metabolism as a transceiver, in comparison to the biological processes. The top pipeline above the dashed line depicts the biological phenomena of a) substrates being absorbed into a biological cell; b) metabolic pathways being triggered by these nutrients; and c) output signals as residues of metabolic activity, such as excreta or biomass growth. The bottom pipeline below the dashed line depicts the abstraction of phenomena in molecular communication where the substrates are reduced to a set of chemical concentrations, the triggered metabolic pathways are reduced to a set of activated reactions, and the perceived outputs are reduced to a set of reaction fluxes for specific biological processes. This abstraction is further discretized into three partitions: Stage I that captures triggering metabolic reactions based on consumed substrates' Stage II that captures perceived outputs based on activated reactions; and end-to-end that captures the full pipeline as the combination of Stages I & II. These partitions are individually examined in this study.

36] were translated and mapped to functions via KEGG [37]. Second, these initial draft GEMs were gap-filled [38] in a media for each consumption profile (2^N differently gap-filled GEMs). This process adds the minimal number of reactions and compounds that enables growth in the parameterized environment. We examined seven compounds ($N = 7$) – glucose (G), hematin (He), formate (F), H_2, Vitamin (B_{12}), acetate (A), and Vitamin K (K) – similar to other studies with these organisms [26,29], yielding $2^7 = 128$ consumption profiles for which IF^* will be computed [28]. A standard base media was additionally used in all simulations, which contained: calcium, chloride ion, carbon dioxide, cobalt, copper, ferrous ion, water, H+, potassium, L-cysteine, magnesium, manganese, sodium, ammonium, nickel, phosphate, sodium bicarbonate, sulfate, zinc, and ferric ion. All lower exchanges bounds were -100 while upper exchange bounds were undefined, thereby granting FBA more freedom to identify the ideal substrate consumption such as those in Table S1. Third, all of the GEMs were simulated through FBA and the flux profiles and objective values were compared and assembled into a single JSON file that was parsed to visualize relationships such as the network comparisons of Hive plots [39] (http://www.hiveplot.com/) in Figures 2 and S7 that better resolve relationships than scatter network plots. Hive plots can moreover compare networks by plotting only the node-edge connections that are common between the networks, which in Figure S8 is the common metabolite-reaction connections between two FBA solution groupings.

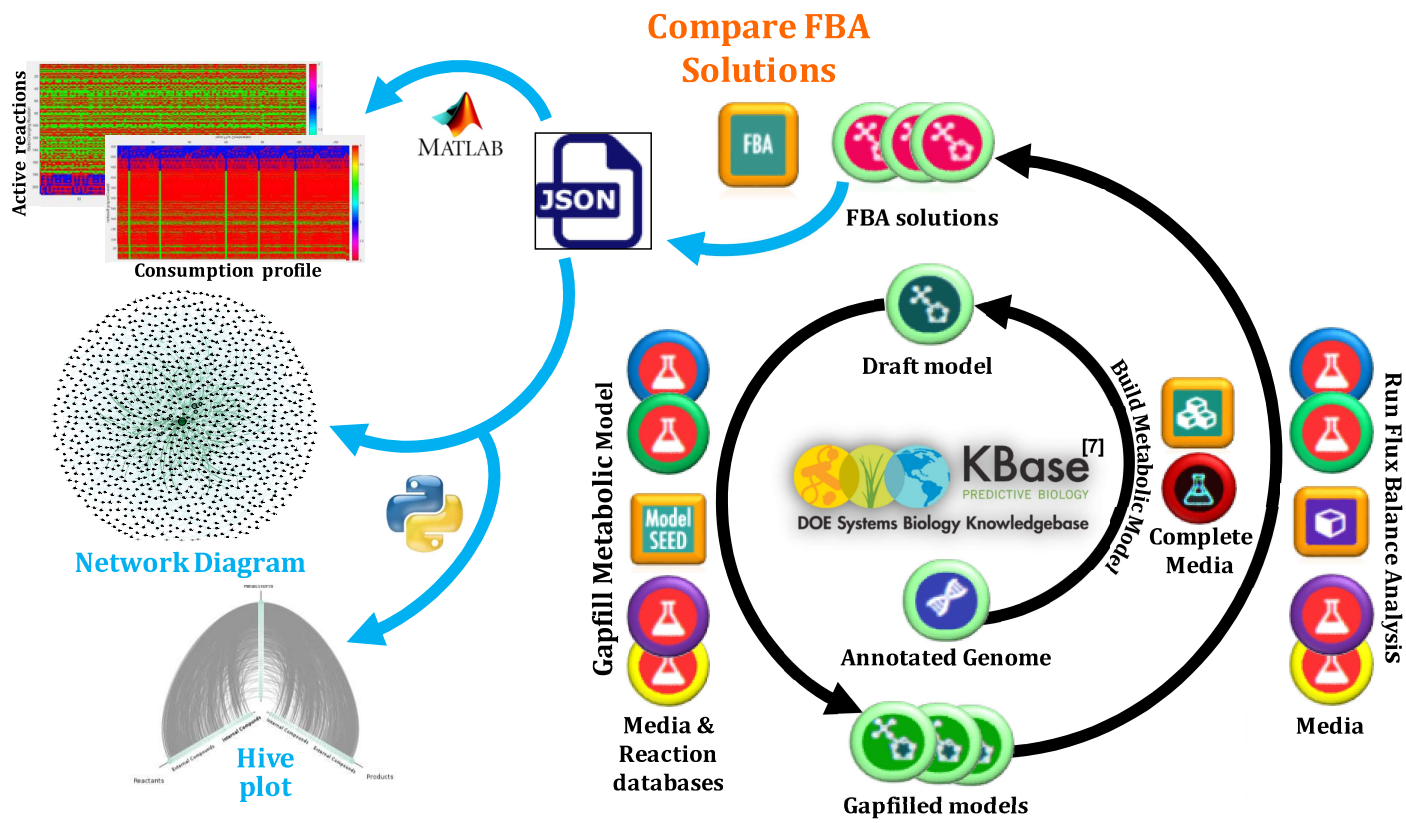

Figure 2: Our modeling workflow, which leverages open-source KBase Applications and custom scripts. The steps that are conducted in KBase include: 1) annotating uploaded genomes, through algorithms such as RAST; 2) constructing draft genome-scale metabolic models (GEMs) from the annotated genomes, via the `Build Metabolic Model` application; 3) gap-filling the draft GEMs to create operational GEMs, via the `Gapfill Metabolic Model` application; 4) acquiring FBA flux profiles in the parameterized media, via the `Run Flux Balance Analysis` application; and then 5) exporting a JSON that compares FBA solutions of the different GEMs and conditions via the `Compare FBA Solutions` application. The exported JSON of compared FBA solutions is subsequently processed through custom MATLAB code into heatmaps that illustrate the sets of activated reactions in each FBA solution and through custom Python scripts that construct network diagrams (each node is a compound whose size is proportional the number of reactions (edges) that connect to it) and hive plots (a three-dimensional plot of reactions on the Z axis, reactants on the X axis, and the products on the Y axis, where substrates are higher in the axes than intra-cellular compounds) to illustrate relationships of the metabolic system.

3 Numerical Results

The maximal information flow IF^* for each channel was determined by computing each term in eq. (1) according to the Stage channels that are defined in eqs. (2) and (3). The presumed equal probability of any given consumption profile for our system of $N = 7$ examined substrates produces $P(\{U_G, U_{He}, U_F, U_{H_2}, U_{B_{12}}, U_A, U_K\}) = 1/128$ for the probability of each consumption profile. The input uncertainty for Stage I from was computed by summing over the 128 inputs in eq. (4) to acquire $H(inputs) = -1 * \log_2(128) = 7\ bits$. The conditional output uncertainty for Stage I of *B. theta* was calculated, from 113 unique reaction activation profiles ($M = 113$) over 14 unique FBA solutions,

$$
\begin{aligned}
H(inputs, outputs) &= \sum (P(inputs, outputs) * \sum (P(inputs, outputs) * \log_2(P(inputs, outputs))) \\
&= -\sum_{e}^{T} (P(e) * \sum_{g,e}^{G,E} (P(e \in g) * \log_2(P(e \in g))) \\
&= -\left[P(FBA_1) * \sum_{e}^{E} (P(FBA_{1e}) log_2(P(FBA_{1e}))) + P(FBA_2) * \sum_{e}^{E} (P(FBA_{2e}) log_2(P(FBA_{2e}))) \right.
\end{aligned}
$$

$$
\begin{aligned}
&+ \cdots + P(FBA_{14}) * \sum_{e}^{E} (P(FBA_{14e}) log_2(P(FBA_{14e})))\Bigg] \\
= &- \Bigg[\frac{6}{128} * (6 * \frac{1}{6} log_2(\frac{1}{6})) + \frac{28}{128} * (28 * \frac{1}{28} log_2(\frac{1}{28})) + 2 * \frac{5}{128} * (5 * \frac{1}{5} log_2(\frac{1}{5})) \\
&+ 2 * \frac{7}{128} * (7 * \frac{1}{7} log_2(\frac{1}{7})) + \frac{32}{128} * (32 * \frac{1}{32} log_2(\frac{1}{32})) + \frac{11}{128} * (11 * \frac{1}{11} log_2(\frac{1}{11})) \\
&+ 2 * \frac{3}{128} * (3 * \frac{1}{3} log_2(\frac{1}{3})) + \frac{9}{128} * (9 * \frac{1}{9} log_2(\frac{1}{9})) + 3 * \frac{4}{128} * (4 * \frac{1}{4} log_2(\frac{1}{4})) \Bigg] \\
= &- [-0.1212 + -1.0516 + -0.1814 + -0.3071 + -1.25 \\
&+ -0.2973 + -0.0743 + -0.2229 + -0.1875] = 3.693 \approx 3.7 \; bits \; ,
\end{aligned}
$$

where the uncertainty of each FBA group is separately calculated and then aggregated into the total output uncertainty. The grouping of the 128 FBA solutions based on reaction fluxes in Figure S4 importantly simplifies the above computation and can facilitate biological investigation in relating consumed substrates to metabolic activation and cellular behaviors. The equivalent probability of a FBA group consumption profile (element e) among all other consumption profiles in the total set of all consumption profiles T or in the same FBA group g – $\frac{1}{T \; or \; g}$ – allows the terms for all elements to be condensed with a coefficient of the number of elements in the group: e.g. the total uncertainty for the 6 elements of FBA group 1 is $\frac{6}{128} * (\mathbf{6} * \frac{1}{6} log_2(\frac{1}{6}))$, where the coefficient **6** collapses the six element terms into a since term. Several FBA groups also possessed the same number of elements, which permitted further simplification with a coefficient of the number of identically sized FBA groups, where all FBA groups are themselves equally probable: e.g. FBA groups 3 and 4 each possess five elements and can therefore be jointly defined as $\mathbf{2} * \frac{5}{128} * (5 * \frac{1}{5} log_2(\frac{1}{5}))$, with the coefficient **2** denoting two FBA groups. The IF^* for Stage I of *B. theta* then equates $H(inputs) - H(inputs, outputs) = 7 - 3.7 = 3.3 \; bits$. The conditional output uncertainty for Stage I of *M. smithii* was computed analogously to the above derivation for *B. theta* to be 2.5 *bits*, except with 136 unique reaction activation profiles ($M = 136$) over 31 unique FBA solutions. The IF^* for Stage I of *B. theta* then equates $7 - 2.5 = 4.5 \; bits$. These results are depicted Figure S9, where *B. theta* reaches its maximum information flow occurs in the absence of formate while *M. smithii* reaches its maximum information flow in the presence of all seven examined substrates.

The FBA groupings that were defined for the Stage I calculations served as the inputs for Stage II and were used to compute the input uncertainty: $-1 * \log_2(14) = 3.8 \; bits$ for *B. theta* and $-1 * \log_2(31) = 5.0 \; bits$ for *M. smithii*. The FBA solutions were then regrouped according to the respective output – Gr ($outputs = Gr$) or both $S_e \; \forall \; e \in E$ and Gr ($outputs = (S_e \; \forall \; e \in E, Gr)$) – to calculate the conditional output uncertainty. The former grouping of $outputs = Gr$ was computed in fig. 3a where the probability of each group g in the set of all FBA groups G is separately evaluated.

$$
\begin{aligned}
H(inputs, outputs) = &\sum (P(inputs, outputs) * \sum (P(inputs, outputs) * \log_2(P(inputs, outputs))) \\
= &- \sum_{g}^{G} (P(g) * \sum_{e}^{E} (P(e \in g) * \log_2(P(e \in g))) \\
= &- \left[4 * \frac{1}{14} * (1 * \frac{1}{1} log_2(\frac{1}{1})) + 3 * \frac{2}{14} * (2 * \frac{1}{2} log_2(\frac{1}{2})) + \frac{4}{14} * (4 * \frac{1}{4} log_2(\frac{1}{4})) \right] \\
= &- [0 + -0.4286 + -0.5714 = 1.000 \approx 1 \; bit \; ,
\end{aligned}
$$

(a) Stage II computation for *B. theta* and $outputs = Gr$

$$
\begin{aligned}
H(inputs, outputs) = &\sum (P(inputs, outputs) * \sum (P(inputs, outputs) * \log_2(P(inputs, outputs))) \\
= &- \sum_{g}^{G} (P(g) * \sum_{e}^{E} (P(e \in g) * \log_2(P(e \in g))) \\
= &- \Bigg[\frac{1}{128} * (1 * \frac{1}{1} log_2(\frac{1}{1})) + \frac{2}{128} * (2 * \frac{1}{2} log_2(\frac{1}{2})) + \frac{5}{128} * (5 * \frac{1}{5} log_2(\frac{1}{5})) \\
&+ \frac{7}{128} * (7 * \frac{1}{7} log_2(\frac{1}{7})) + 7 * \frac{8}{128} * (8 * \frac{1}{8} log_2(\frac{1}{8})) + \frac{9}{128} * (9 * \frac{1}{9} log_2(\frac{1}{9})) \\
&+ 3 * \frac{16}{128} * (16 * \frac{1}{16} log_2(\frac{1}{16})) \Bigg] \\
= &- [0 + -0.0156 + -0.0907 + -0.1535 + -1.3125 + -0.2229 + -2.585] = 3.2952 \approx 3.3 \; bits
\end{aligned}
$$

(b) End-to-end computation for *M. smithii* and $outputs = Gr$

Figure 3: IF^* computations for Stage II and end-to-end channels for the two examined organisms.

The Stage II information flow with biomass growth as the observed output is therefore $IF^* = 3.8 - 1 = 2.8 \; bits$. The analogous computation for *M. smithii* resulted in $IF^* = 5 - 1.1 = 3.9 \; bits$. The second FBA grouping by both excretions and biomass manifested in $IF^* = 3.8 - .1 = 3.7$ for *B. theta* and $IF^* = 5.0 - 1.1 = 3.9$ for *M. smithii*. The increase in IF^* for *B. theta* when including metabolic excretion is intuitive, since more outcomes are externally perceived; however, the unchanged value of *M. smithii*, and modest increase in *B. theta*, suggests that biomass growth captures most of the information flow during substrate consumption. The end-to-end channel – $inputs = 128 \; consumption \; profiles$, $outputs = Gr$, and FBA groups according to Gr – was finally computed to be $IF^* = 7 - 4.3 = 2.7 \; bits$ for *B. theta* and $IF^* = 7 - 3.3 = 3.7 \; bits$ for *M. smithii* in Figure S10, where the conditional output was computed in fig. 3b for *M. smithii*.

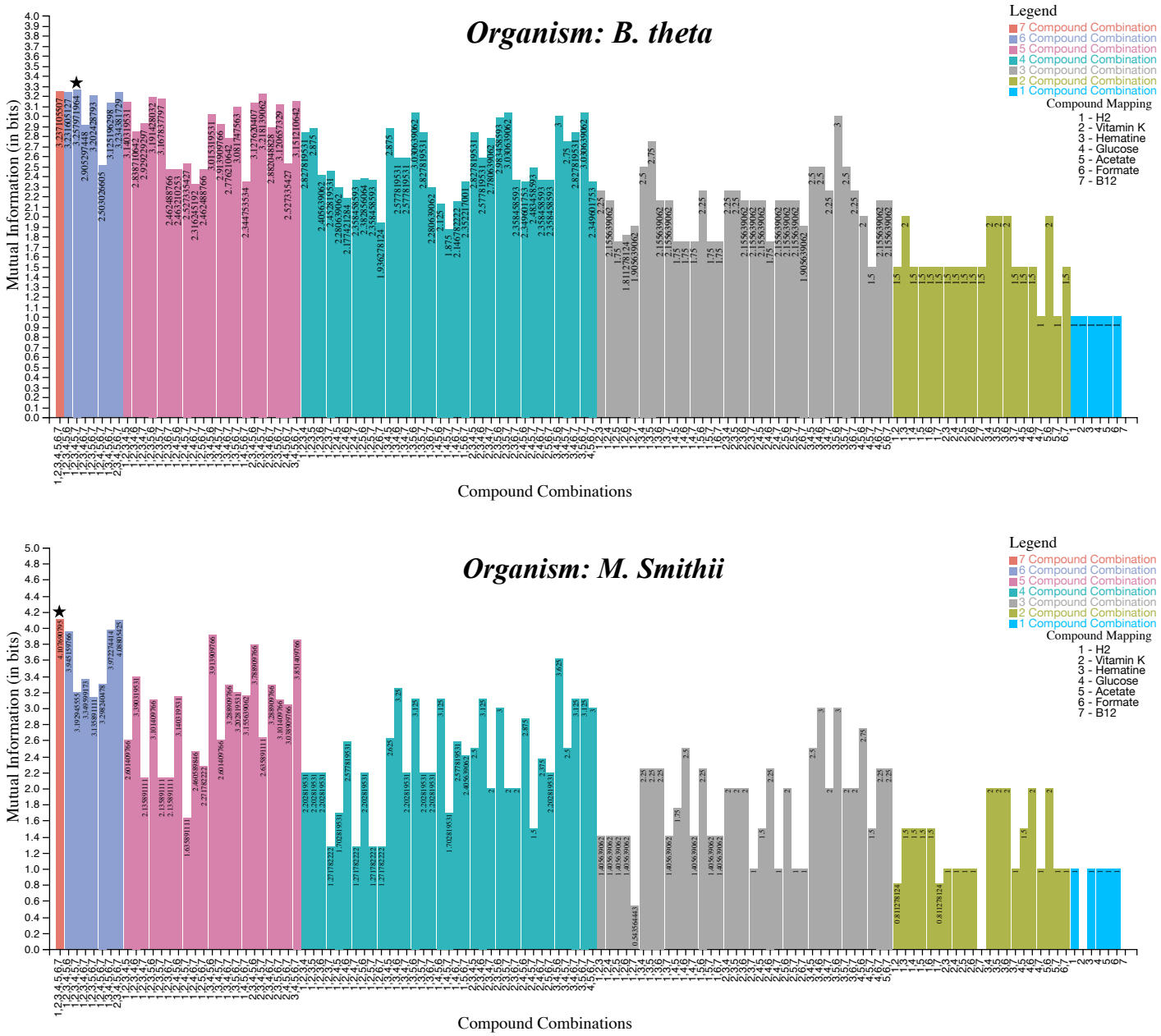

Figure 4: The end-to-end upper bounds for each consumption profile. The maximal information flow is starred. The consumption profiles with more compounds predictably manifested in greater potential information flow. The included substrates in each examined profile are condensed on the x-axis with numbering: 1 = glucose (G), 2 = hematin (He), 3 = formate (F), 4 = H_2, 5 = Vitamin (B_{12}), 6 = acetate (A), and 7 = Vitamin K (K).

3.1 Visualizations

The constellation diagrams of Figure 5 statistically compress the 128 possible consumption profiles into a tangible figure for rapid interpretation. These diagrams were constructed by first: 1) grouping consumption profiles by IF^* from the end-to-end channel; 2) determining the minimum and maximum IF^* for each consumption profile; and 3) graphing each of the minimum, maximum, and average IF^* (excluding the minimum and maximum) per the size of the consumption profile. These diagrams interestingly revealed that the maximum IF^* begins to plateau with consuming ≥ 5 of the examined compounds, which suggests that there are diminishing returns to cellular control from environmental perturbations. This trend is consistent with the BioSIMP software that was used to identify the environmental nutritional factors required for growth of *B. theta* and *M. smithii* [29]. This trend is moreover echoed by Figures 4, S9, and S10 that reveal some consumption profiles that exhibit remarkably high IF^* from less than half of the examined compounds: e.g. F, B_{12}, A for *B. theta* and *M. smithii* or F, H_2, A for *M. smithii*. This basic knowledge of infor-

mation flow under variable conditions would be necessary for biomedical monitoring and other systems that require molecular transport to characterize metabolic state.

4 Conclusions and Future Work

Molecular communication theory quantifies the flow of information (in bits) that cells can encode from their environments into metabolic activity, substrate excretions, or biomass growth. We materialized this concept into a model that couples conventional FBA with MC theory and several black-box communication channels of metabolism whose outputs are intra-cellular reaction activity, metabolite excretion, or biomass growth. The quantification of information flow from our model identified the consumption profiles that optimally transmit information across noisy biochemistry and manifest cellular outcomes, which can potentially minimize the number of resource-intensive experiments that are necessary to find substrates that desirably control cellular behaviors. The use of FBA further identifies the theoretical limit of information flow, and thus environmental control, from substrate perturbations. We further developed visualizations, such as hive plots and a novel use of constellation diagrams, that succinctly communicate information flow and network connectivity to facilitate interpretation by investigators. Code, KBase Narratives, and additional details are available in our GitHub repository (https://github.com/freiburgermsu/MetabolicMC_Supplementary_Git_v1). This model advances basic biological knowledge of cellular engagement with its environment, and provides a tool to identify substrates that can most effectively engineering cellular behavior from media perturbations or monitor cellular metabolism, with diverse applications in biomedical wearable technologies or ecological control through benign substrate perturbations. Subsequent work will refine our model by 1) better compensating biochemical noise; 2) capturing dynamic information flows and continuous variables via the dynamic FBA algorithm; 3) validating predictions with experimental data; and 4) empowering autonomous laboratories to monitor and control cellular behaviors based on information transmission.

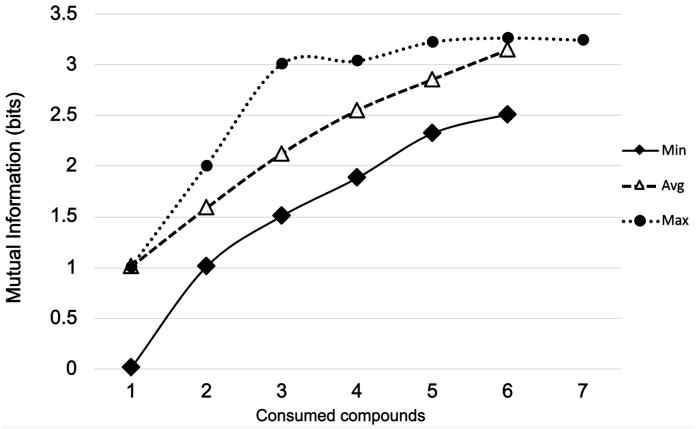

(a) *B. theta*

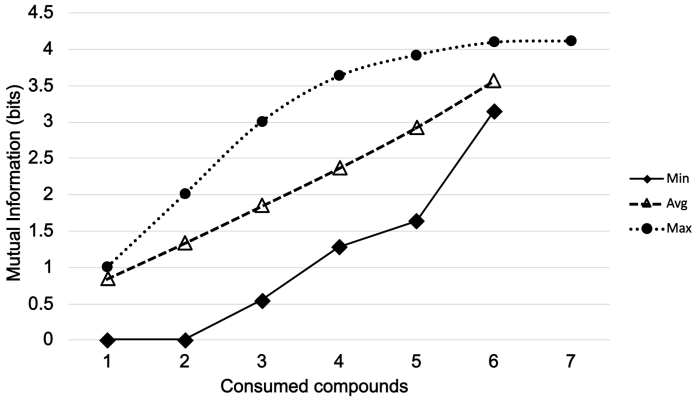

(b) *M. smithii*

Figure 5: Constellation diagrams for the information flow from all consumption profiles in the total end-to-end abstraction. The minimum, maximum, and average values are plotted against the number of compounds in the consumption profiles, which reveals that the maximum information flow increases logarithmically while the average information flow increases linearly. This observation is intuitive where inherent noise or otherwise defines a fundamental limit to information flow but generally an increase in the considered dimensions (consumed compounds) increases the uncertainty (information flow) of the system.

Acknowledgment

This work was funded by the US National Science Foundation through grant MCB-1449014, the National Institutes of Health 11-P20-GM113126-01, hi Sa the NSF EPSCoR EPS-1004094 and the CCF-1161767. Also the grant supported by NIH 11-P20-GM113126-01. The authors would also like to thank KBase developers for their active support throughout the development of this research.

Conflict of interest

The authors declare no conflict of interest with the presented work.

References

[1] I. Akyildiz, M. Pierobon, S. Balasubramaniam, and Y. Koucheryavy, "The internet of bio-nano things," *IEEE Communications Magazine*, vol. 53, no. 3, pp. 32–40, 2015.

[2] I. F. Akyildiz, J. M. Jornet, M. Pierobon, and S. Balasubramaniam, "Moving forward with molecular communication: From theory to human health applications," *Proceedings of the IEEE*, vol. 107, pp. 858–865, May 2019.

[3] W. A. Lim, "The promise of optogenetics in cell biology: interrogating molecular circuits in space and time," *Nature Reviews*, vol. 11, pp. 393–403, 2010.

[4] J. E. Toettcher, C. A. Voigt, O. D. Weiner, and W. A. Lim, "The promise of optogenetics in cell biology: interrogating molecular circuits in space and time," *Nature Methods*, vol. 8, pp. 35–38, 2011.

[5] J. Dobson, "Remote control of cellular behaviour with magnetic nanoparticles," *Nature Nanotechnology*, vol. 3, pp. 139–143, 2008.

[6] E. Gonçalves, J. Bucher, A. Ryll, J. Niklas, K. Mauch, S. Klamt, M. Rocha, and J. Saez-Rodriguez, "Bridging the layers: towards integration of signal transduction, regulation and metabolism into mathematical models," *Molecular BioSystems*, vol. 9, no. 7, pp. 1576–1583, 2013.

[7] A. F. Villaverde and J. R. Banga, "Reverse engineering and identification in systems biology: strategies, perspectives and challenges," *Journal of The Royal Society Interface*, vol. 11, no. 91, p. 20130505, 2014.

[8] D. M. Klurfeld, C. D. Davis, R. W. Karp, E. Allen-Vercoe, E. B. Chang, B. Chassaing, G. C. Fahey, B. R. Hamaker, H. D. Holscher, J. W. Lampe, A. Marette, E. Martens, S. J. O, D. J. Rose, M. Saarela, B. O. Schneeman, J. L. Slavin, J. L. Sonnenburg, K. S. Swanson, G. D. Wu, C. J. Lynch, and F. G. Jr, "Considerations for best practices in studies of fiber or other dietary components and the intestinal microbiome," *Am J Physiol Endocrinol Metab*, vol. 315, pp. 1087–1097, 2018.

[9] N. Fei, S. Miyoshi, J. B. Hermanson, J. Miyoshi, B. Xie, O. Deleon, M. Hawkins, W. Charlton, M. D. Souza, J. Hart, D. Sulakhe, K. B. Martinez-Guryn, E. B. Chang, M. R. Charlton, and V. A. Leone, "Imbalanced gut microbiota predicts and drives the progression of nonalcoholic fatty liver disease and nonalcoholic steatohepatitis in a fast-food diet mouse model," *bioRxiv*, 2023.

[10] C. M. Metallo and M. G. V. Heiden, "Understanding metabolic regulation and its influence on cell physiology," *Molecular Cell*, vol. 49, pp. 388–398, February 2013.

[11] D. L. Nelson and M. M. Cox, *Lehninger Principles of Biochemistry*, ch. 12.2, pp. 425–429. W. H. Freeman, 2005.

[12] N. Campbell and J. Reece, "Biology 7th edition, ap," 2005.

[13] O. S. Soyer, M. Salathe, and S. Bonhoeffer, "Signal transduction networks: topology, response and biochemical processes," *Journal of Theoretical Biology*, vol. 238, no. 2, pp. 416–425, 2006.

[14] C. J. Myers, *Engineering genetic circuits*. Chapman & Hall/CRC, Mathematical and Computational Biology Series, 2009.

[15] T. M. Cover and J. A. Thomas, *Elements of Information Theory, 2nd Edition*. Wiley, 2006.

[16] F. Fabris, "Shannon information theory and molecular biology," *Journal of Interdisciplinary Mathematics*, vol. 12, no. 1, pp. 41–87, 2009.

[17] I. F. Akyildiz, J. M. Jornet, M. Pierobon, and S. Balasubramaniam, "An information theoretic framework to analyze molecular communication systems based on statistical mechanics," *Proceedings of the IEEE*, vol. 107, pp. 1230–1255, July 2019.

[18] A. Rhee, R. Cheong, and A. Levchenko, "The application of information theory to biochemical signaling systems," *Phys Biol.*, vol. 9, p. 045011, August 2012.

[19] K. R. Gorla and M. Pierobon, "A mutual information estimate for a redox-based molecular-electrical communication channel," Association for Computing Machinery, Inc, 9 2021.

[20] K. Höffner, S. Harwood, and P. Barton, "A reliable simulator for dynamic flux balance analysis," *Biotechnology and bioengineering*, vol. 110, no. 3, pp. 792–802, 2013.

[21] E. H. Davidson, *The regulatory genome: gene regulatory networks in development and evolution*. Academic press, 2010.

[22] J. D. Orth, I. Thiele, and B. Ø. Palsson, "What is flux balance analysis?," *Nature biotechnology*, vol. 28, no. 3, pp. 245–248, 2010.

[23] C. S. Henry, L. J. Broadbelt, and V. Hatzimanikatis, "Thermodynamics-based metabolic flux analysis," *Biophysical Journal*, vol. 92, no. 5, pp. 1792–1805, 2007.

[24] M. W. Covert, C. H. Schilling, and B. Palsson, "Regulation of gene expression in flux balance models of metabolism," *Journal of Theoretical Biology*, vol. 213, pp. 73–88, 2001.

[25] Z. Sakkaff, J. L. Catlett, M. Cashman, M. Pierobon, N. R. Buan, M. B. Cohen, and C. A. Kelley, "End-to-end molecular communication channels in cell metabolism: an information theoretic study," in *Proceedings of the 4th ACM International Conference on Nanoscale Computing and Communication (ACM NanoCom)*, September 2017.

[26] J. L. Catlett, S. Carr, M. Cashman, M. D. Smith, M. Walter, Z. Sakkaff, C. Kelley, M. Pierobon, M. B. Cohen, and N. R. Buan, "Metabolic synergy between human symbionts bacteroides and methanobrevibacter," *Microbiology Spectrum*, vol. 10, 6 2022.

[27] M. Cashman, J. L. Catlett, M. B. Cohen, N. Buan, Z. Sakkaff, M. Pierobon, and C. Kelley, "Sampling and Inference in Configurable Biological Systems: A Software Testing Perspective," Tech. Rep. TR-UNL-CSE-2016-0007, University of Nebraska-Lincoln, 2016.

[28] M. Pierobon, M. B. Cohen, N. Buan, and C. Kelley, "SCIM: Sampling, Characterization, Inference and Modeling of Biological Consortia," Tech. Rep. TR-UNL-CSE-2015-0002, University of Nebraska-Lincoln, 2015.

[29] M. Cashman, J. L. Catlett, M. B. Cohen, N. R. Buan, Z. Sakkaff, M. Pierobon, and C. A. Kelley, "Biosimp: using software testing techniques for sampling and inference in biological organisms," in *2017 IEEE/ACM 12th International Workshop on Software Engineering for Science (SE4Science)*, pp. 2–8, IEEE, 2017.

[30] R. Togneri and J. Christopher, *Fundamentals of information theory and coding design*. CRC Press, 2003.

[31] Lehner, "To new frontiers, microbiology for nanotechnology and space exploration," 2019.

[32] A. J. Berliner, J. M. Hilzinger, A. J. Abel, M. J. McNulty, G. Makrygiorgos, N. J. Averesch, S. S. Gupta, A. Benvenuti, D. F. Caddell, S. Cestellos-Blanco, A. Doloman, S. Friedline, D. Ho, W. Gu, A. Hill, P. Kusuma, I. Lipsky, M. Mirkovic, J. L. Meraz, V. Pane, K. B. Sander, F. Shi, J. M. Skerker, A. Styer, K. Valgardson, K. Wetmore, S. G. Woo, Y. Xiong, K. Yates, C. Zhang, S. Zhen, B. Bugbee, D. S. Clark, D. Coleman-Derr, A. Mesbah, S. Nandi, R. M. Waymouth, P. Yang, C. S. Criddle, K. A. McDonald, L. C. Seefeldt, A. A. Menezes, and A. P. Arkin, "Towards a biomanufactory on mars," *Frontiers in Astronomy and Space Sciences*, vol. 8, 7 2021.

[33] G. J. Baart and D. E. Martens, "Genome-scale metabolic models: reconstruction and analysis," *Neisseria meningitidis: Advanced Methods and Protocols*, pp. 107–126, 2012.

[34] KBase, "Department of Energy Systems Biology Knowledgebase (KBase)." http://kbase.us. [Online; accessed 22-September-2016].

[35] A. Sheydina, R. Y. Eberhardt, D. J. Rigden, Y. Chang, Z. Li, C. C. Zmasek, H. L. Axelrod, and A. Godzik, "Structural genomics analysis of uncharacterized protein families overrepresented in human gut bacteria identifies a novel glycoside hydrolase," *BMC bioinformatics*, vol. 15, no. 1, p. 1, 2014.

[36] M. Zhou, Y.-H. Chung, K. Beauchemin, L. Holtshausen, M. Oba, T. McAllister, and L. Guan, "Relationship between rumen methanogens and methane production in dairy cows fed diets supplemented with a feed enzyme additive," *Journal of applied microbiology*, vol. 111, no. 5, pp. 1148–1158, 2011.

[37] KEGG, "Kyoto encyclopedia of genes and genomes (KEGG)." http://www.genome.jp/kegg/. [Online; accessed 22-September-2016].

[38] C. S. Henry, M. DeJongh, A. A. Best, P. M. Frybarger, B. Linsay, and R. L. Stevens, "High-throughput generation, optimization and analysis of genome-scale metabolic models," *Nature biotechnology*, vol. 28, no. 9, pp. 977–982, 2010.

[39] M. Krzywinski, I. Birol, S. J. Jones, and M. A. Marra, "Hive plots—rational approach to visualizing networks," *Briefings in bioinformatics*, vol. 13, no. 5, pp. 627–644, 2012.

Supplementary Information

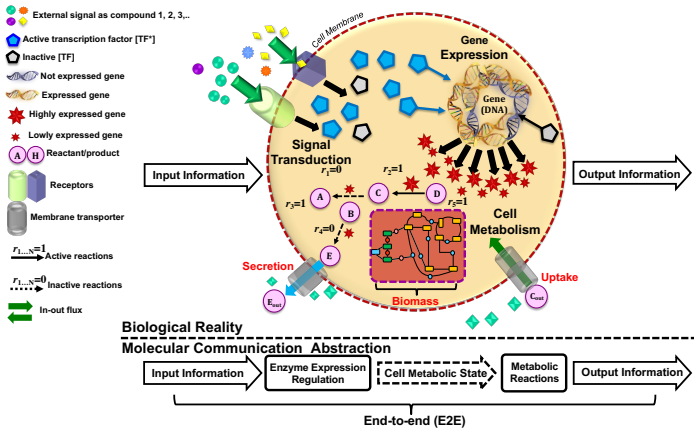

Figure S1: Biological reality of Molecular communication in cell metabolism.

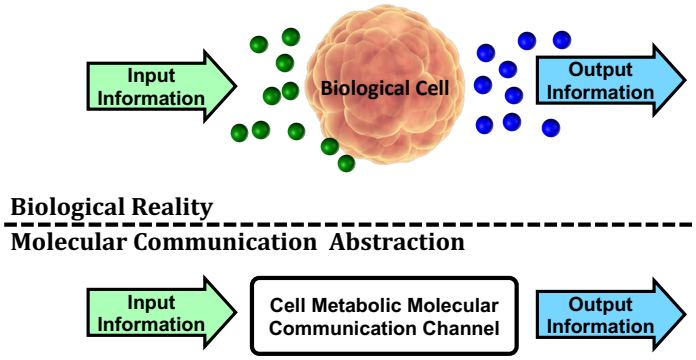

(a) Overview of biological realm and molecular communication abstraction.

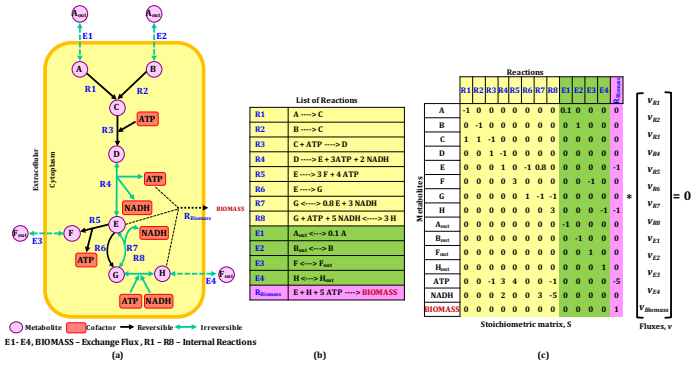

(b) From metabolic network to stoichiometric matrix. (a) shows a conceptual model of a metabolic network where the internal chemical reactions are represented by R_i. (b) shows the exchange fluxes with the environment labeled as E_j. (c) shows the stoichiometric matrix S where each row corresponds to a chemical compound in the metabolic network, while each column corresponds to the reaction or flux exchanged with the environment. Each entry of the stoichiometric matrix S is the stoichiometric coefficient that indicates how many molecules of a chemical compound, represented by row entry, are consumed (coefficient < 0) or produced (coefficient > 0) in one of the possible reactions.

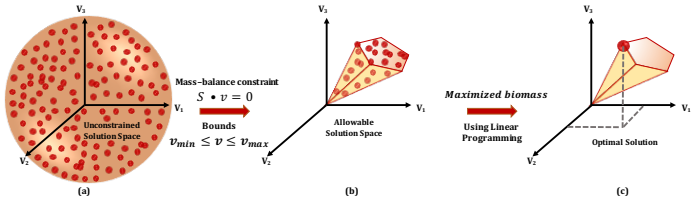

(c) Conceptual model of the FBA linear program formulation for finding the optimal solution. Optimization of the objective function $a'\mathbf{v}$ identifies a flux distribution on the edge of the allowable solution space.

Figure S2: Background information on a) the molecular communication abstraction of cellular systems, where cellular metabolism is black-boxed; b) the FBA algorithm and its use of matrix algebra; and c) the geometric solution space that linear optimization in FBA navigates to find the optimal solution.

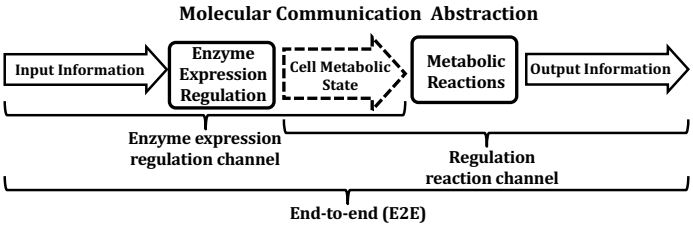

Figure S3: Molecular communication channel abstraction of cell metabolism.

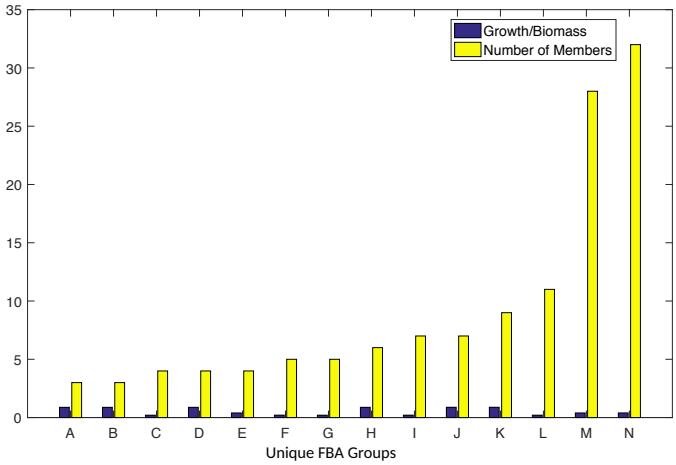

(a) 14 unique FBA groups for *B. theta*

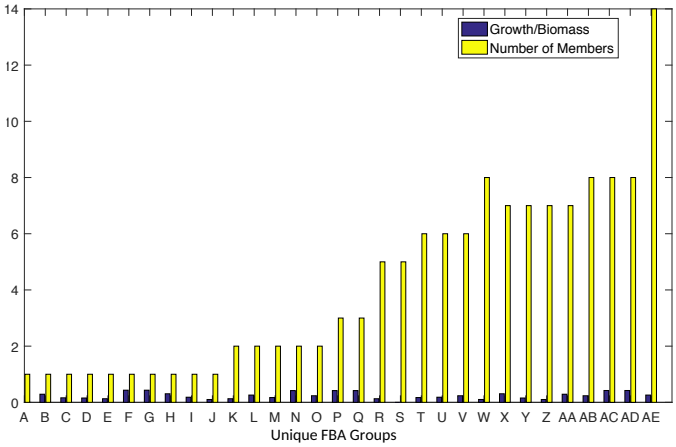

(b) 31 unique FBA groups for *M. smithii*

Figure S4: The number of FBA solutions per group of unique activation profiles, over all consumption profiles. The *M. smithii* metabolism exhibited more than twice as many unique metabolic responses to the consumption profiles than *B. theta*, which suggests that it is more dynamic to its environment. This is corroborated by the much higher proportion of active reactions in Figure S5 relative to *B. theta*.

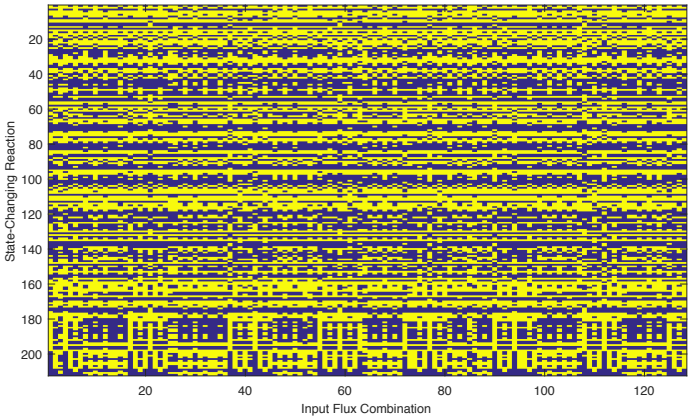

(a) *B. theta*

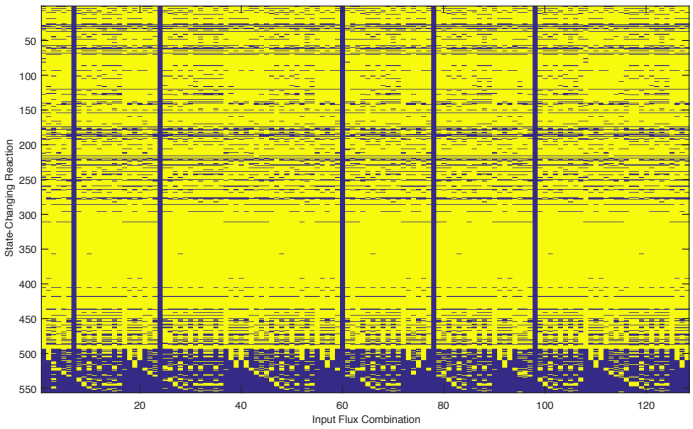

(b) *M. smithii*

Figure S5: Reaction activation from FBA simulations $\{r_i^*\}_{i=1}^M$ for each possible consumption profile, where yellow is active and violet is inactive. *M. smithii* metabolism is evidently much more activated than *B. theta* by the examined media, notwithstanding a handful of media profiles that did not support growth (illustrated as vertical lines), although *B. theta* seems to have exhibited at least some metabolic activation in all of the examined media. This may be the consequence of *B. theta* utilizing anaerobic fermentation that expands its habitable zone beyond that of *M. smithii*.

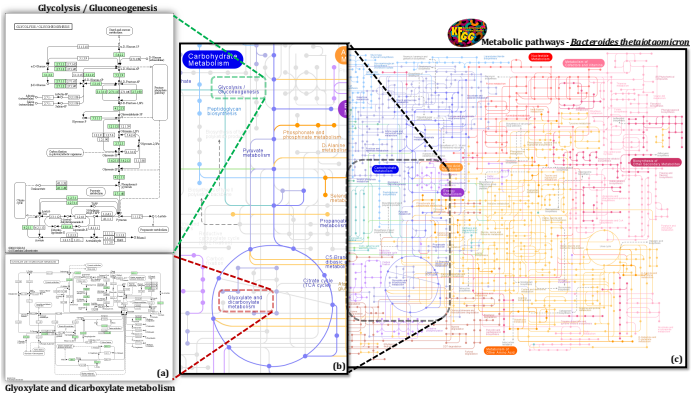

Figure S6: KEGG module of *Bacteroides thetaiotaomicron* metabolic pathways. **(a)** Summary of the biological processes shown in the pathway map of Glycolysis / Gluconeogenesis and Glyoxylate and dicarboxylate metabolism. **(b)** Enlarged fine details of a section of a complete metabolic model. **(c)** Part of the complete KEGG database pathway maps of *Bacteroides thetaiotaomicron*. visualized parts of a GEM (on the right) for the organisms *B. theta*, used in our study, which is obtained from the Kyoto Encyclopedia of Genes and Genomes (KEGG) database [37]. The nodes represent compounds that are inputs/outputs to the reactions, and edges represent the chemical reactions. Inputs from the environment taken by the organism are involved in the reactions of metabolic pathways, resulting in the exchange of fluxes with the environment (uptake and secretion) or in the production of biomass (growth).

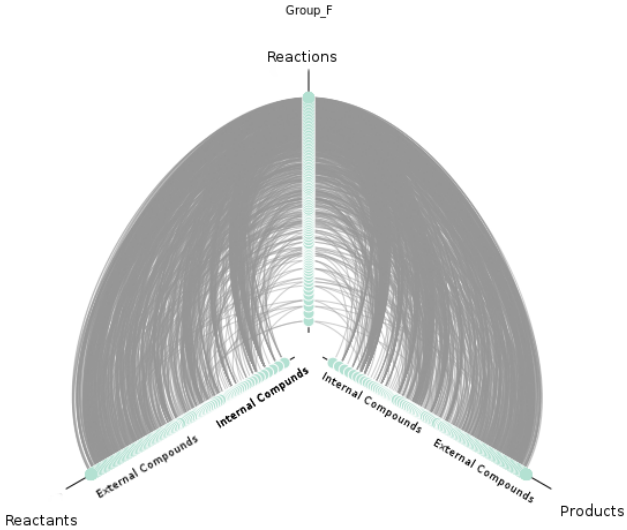

Figure S7: A hive plot for a configuration F is shown in the figure. The reactions are placed on the Z axis, the reactants on the X axis and the products on the Y axis. Further the External compounds are placed higher on the X and Y axes than the Internal compounds.

Table S1: $\mathbf{v_{max}}$ of minimal media compounds and important 7 compounds.

Compound Name	MaxFlux (mmol/g CDW/hr)
Calcium (Ca^{2+})	0.180254
Chloride (Cl^{-})	16.058
Carbon dioxide ($C0_2$)	34.00204
Cobalt (Co^{2+})	0.042029
Copper (Cu^{2+})	1
Ferrous (Fe^{2+})	0.014
H^+	1
Water (H_2O)	46166.89
Potassium (K^+)	100
L − Cysteine	2.8
Magnesium (Mg)	0.098375
Manganese (Mn^{2+})	0.050529
Sodium (Na^+)	17.564
Ammonium (NH_3)	7.5
Nickel (Ni^{2+})	1
Phosphate	100
Sodium bicarbonate	11.9
Sulfate	7.5
Zinc (Zn^{2+})	1
Ferric (Fe^{3+})	0.014
D-Glucose	2.78
Hematin	0.02
Formate	10
H_2	0.78000078
Vitamin B12	0.0000037
Acetate	10
Vitamin K	5.8

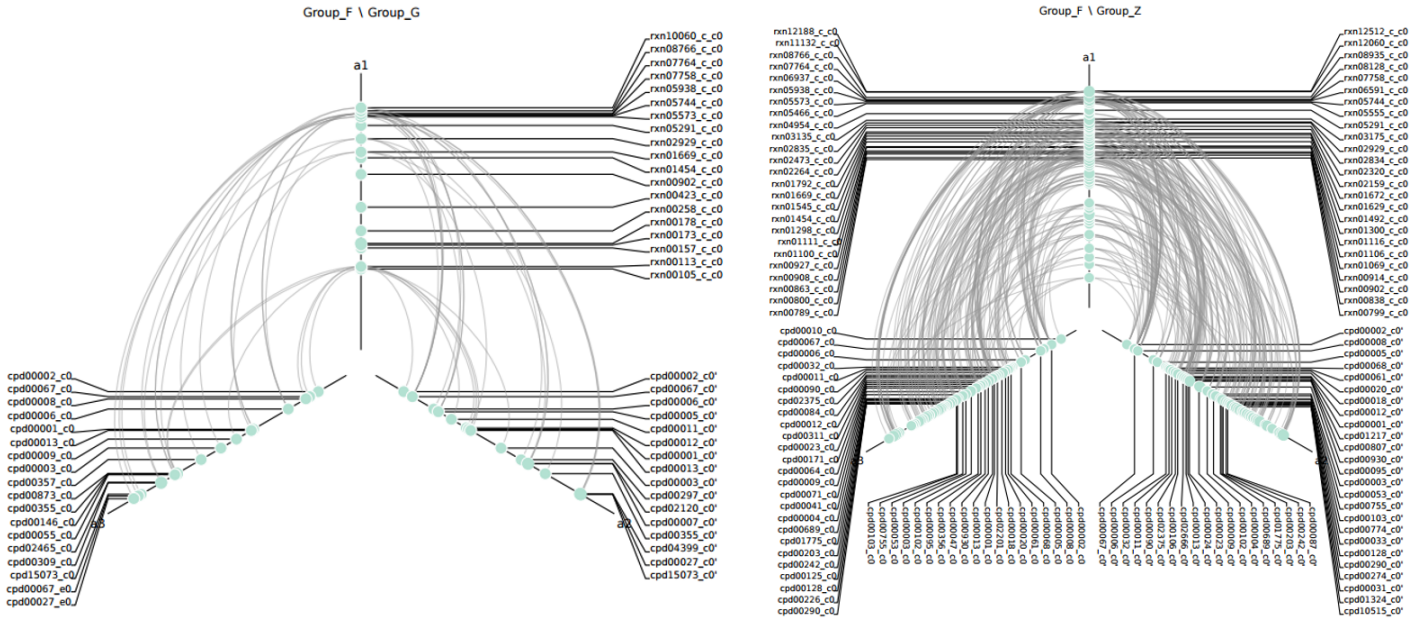

Figure S8: In this figure we take 3 different configuration of state changing reactions, labelled F, G and Z. It shows differential hive plots of F vs G and F vs Z. The groups F and G in F vs G hive plot has the same biomass whereas, the groups F and Z in F vz Z hive plot have the least and highest biomass respectively. When a reaction is present in F and absent in G or Z the reaction is represented along with its links to the compounds. When a reaction is present in the other groups but absent in group F the reaction is shown as a node not connected to any other compounds.

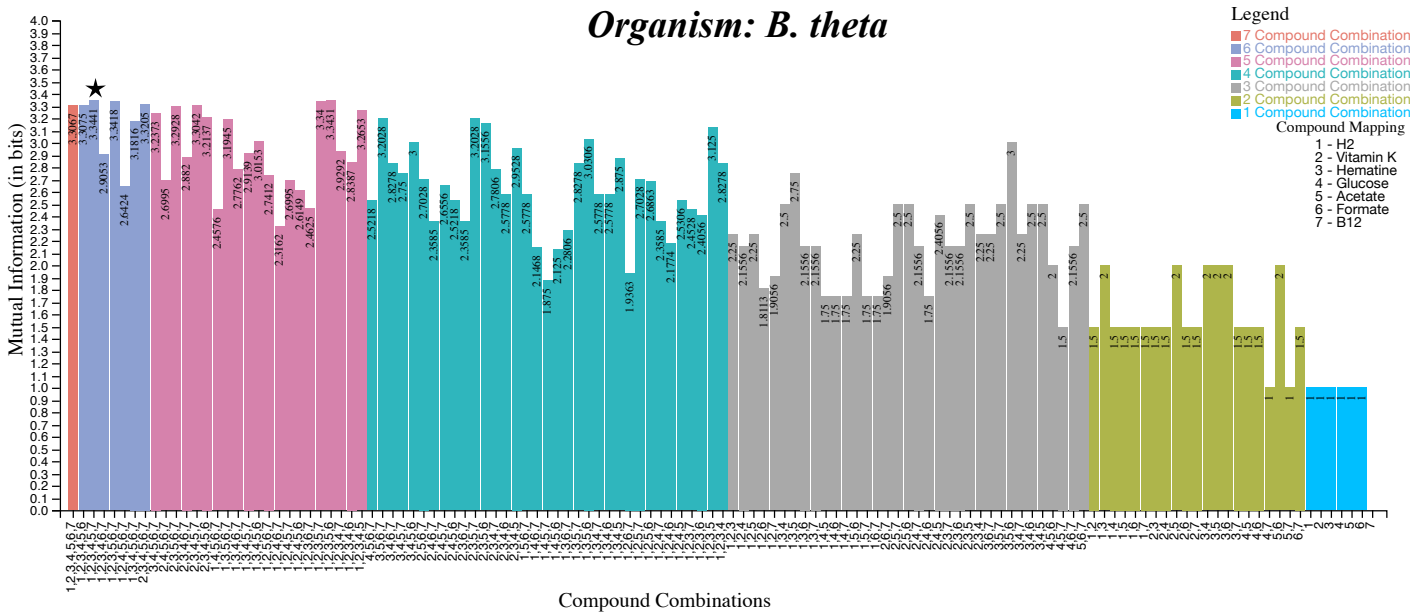

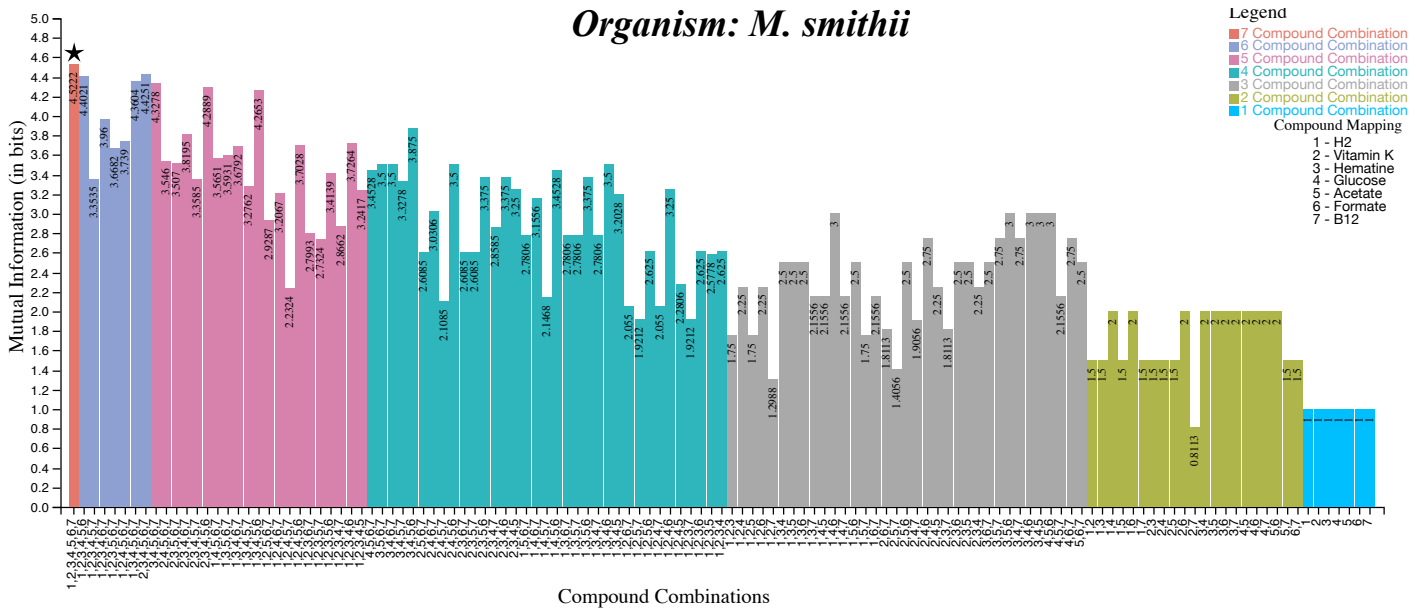

Figure S9: Upper bounds of the steady-state mutual information for all the different combinations of seven compounds in Enzyme Expression Regulation channel in . The best estimation of the maximum information is starred.

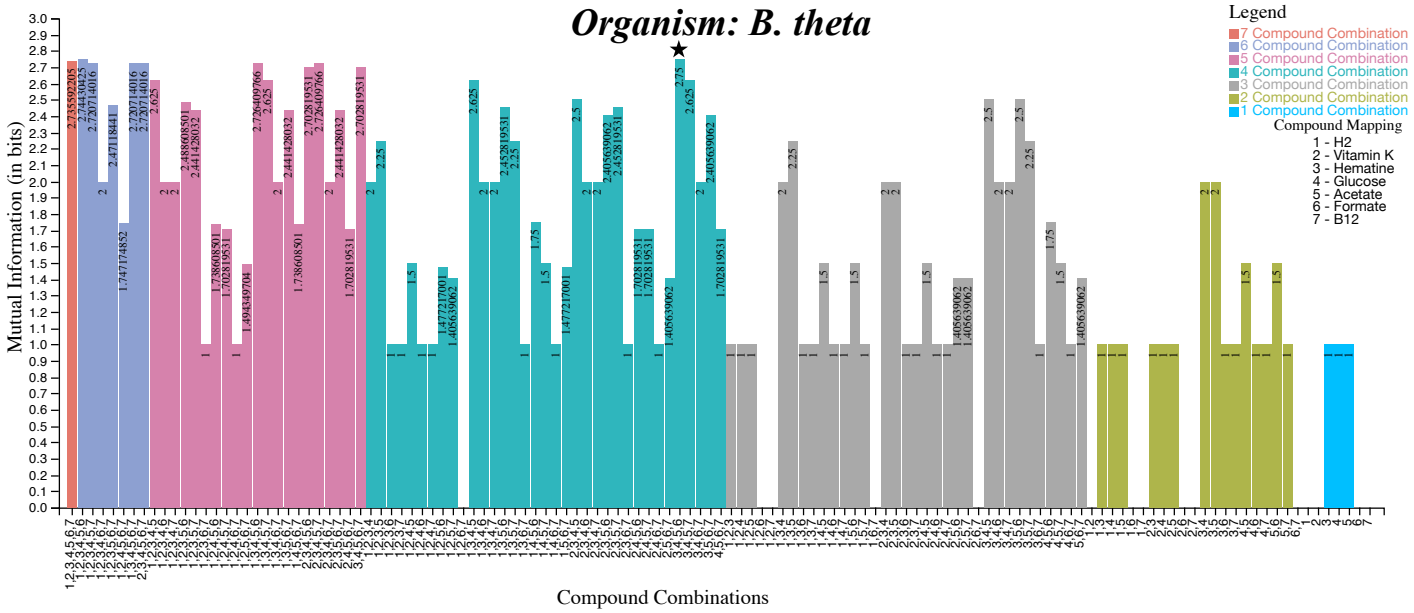

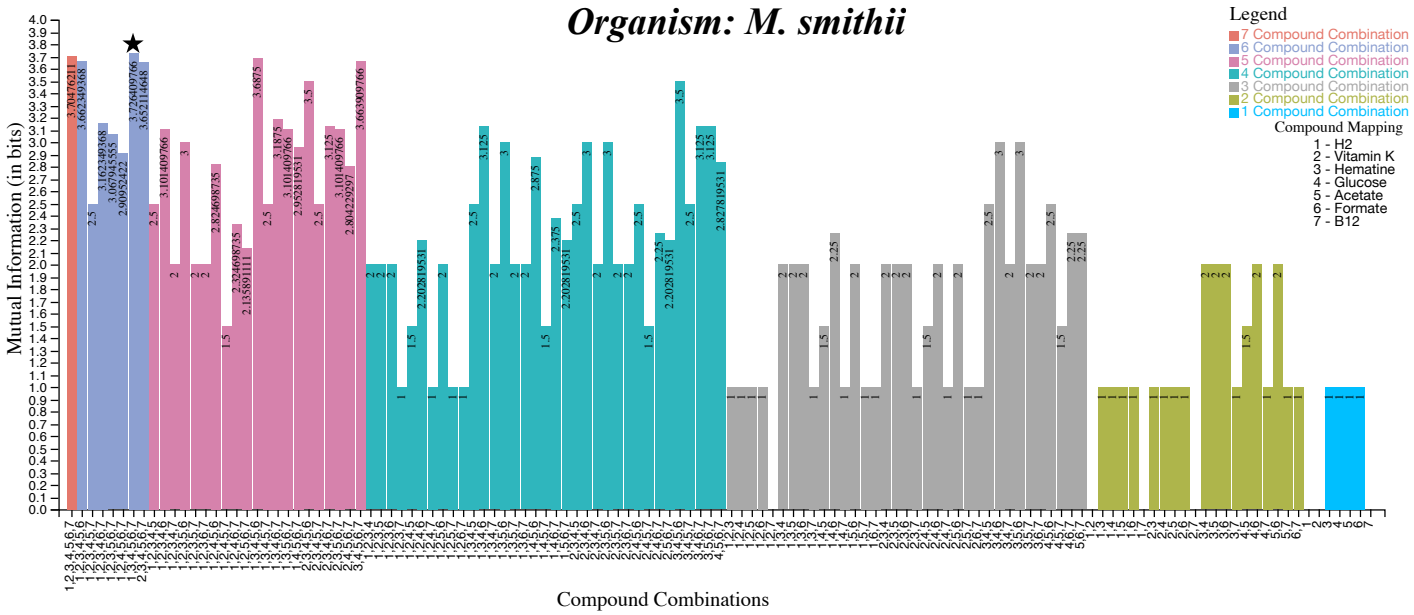

Figure S10: Upper bounds of the steady-state mutual information for all the different combinations of seven compounds in E2E in with respect to **Biomass only**. The best estimation of the maximum information is starred.

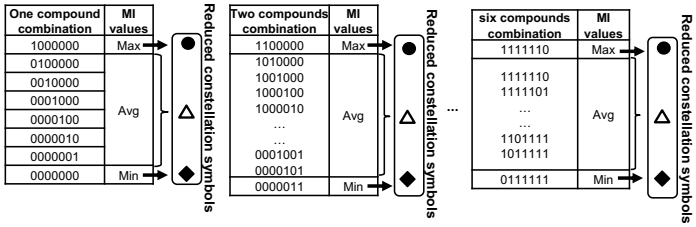

Figure S11: Steps involved in constructing constellation diagram.